Received: 7 August 2023 | Revised: 30 January 2024 | Accepted: 13 February 2024

DOI: 10.1002/mawe.202300217

ARTICLE

WILEY VCH

The effect of tempering time and cooling environment on the corrosion behavior of AA5083-H111 alloy

Der Einfluss der Anlasszeit und der Abkühlumgebung auf das Korrosionsverhalten der Aluminiumlegierung AA5083-H111

İ. Karagöz[1] | **M. Buğdaycı**[2, 3] | **L. Öncel**[4]

[1]Department of Polymer Materials Engineering, Faculty of Engineering, Yalova University, Yalova, Türkiye

[2]Department of Chemical Engineering, Faculty of Engineering, Yalova University, Yalova, Türkiye

[3]Department of Construction Technology, Vocational School, Istanbul Medipol University, İstanbul, Türkiye

[4]Department of Metallurgical and Materials Engineering, Faculty of Engineering and Architecture, Sinop University, Sinop, Türkiye

Correspondence
İ. Karagöz, Department of Polymer Materials Engineering, Faculty of Engineering, Yalova University, Yalova 77200, Türkiye.
Email: idris.karagoz@yalova.edu.tr

Abstract

The tempering process can increase the mechanical properties of the material, such as hardness and impact strength, as well as enhance the corrosion resistance. Therefore, the selection of appropriate tempering time and cooling environment is crucial. This study aims to investigate changes in properties such as hardness, tensile strength, corrosion resistance, and microstructure of AA5083-H111 alloy after a brief tempering process (30 minutes, 45 minutes and 60 minutes) at 320 °C, followed by cooling in air and water environments. The study found that tempering time and cooling environment significantly affect the mechanical properties and corrosion rate. The results show that samples labeled as S30 and S60 have the highest hardness and impact strength, but the best corrosion resistance is achieved in the S60 sample. This study demonstrates that even after a limited-term tempering process, the mechanical properties and corrosion resistance of AA5083-H111 alloy can be improved. This information is crucial data for use in the production and application of alloys. The findings of this study could have important implications for the production and application of AA5083-H111 alloy in industries such as aerospace, automotive, and marine engineering.

KEYWORDS

AA5083-h111 alloy, cooling environment, corrosion behaviour, corrosion resistance, microstructure, shot-term tempering process

Abstract

Der Anlassprozess kann die mechanischen Eigenschaften des Werkstoffes wie Härte und Schlagfestigkeit verbessern und gleichzeitig die Korrosionsbeständigkeit erhöhen. Dafür ist die Auswahl der geeigneten Anlasszeit und der Kühlumgebung entscheidend. Diese Studie zielt darauf ab, die Veränderungen der Eigenschaften wie Härte, Zugfestigkeit, Korrosionsbeständigkeit und Gefüge der AA5083-H111 Legierung nach einem kurzfristigen Anlassprozess

(30 Minuten, 45 Minuten und 60 Minuten) bei 320 °C und anschließender Abkühlung in Luft- und Wasserumgebungen zu untersuchen. Die Studie hat herausgefunden, dass die Anlasszeit und die Kühlumgebung einen Einfluss auf die mechanischen Eigenschaften und die Korrosionsrate haben. Die Ergebnisse zeigen, dass die Proben mit den Bezeichnungen S30 und S60 die höchste Härte und Schlagfestigkeit aufweisen, aber die beste Korrosionsbeständigkeit in der Probe S60 erreicht wird. Diese Studie zeigt, dass selbst nach einem kurzfristigen Anlassprozess die mechanischen Eigenschaften und die Korrosionsbeständigkeit der AA5083-H111 Legierung verbessert werden können. Diese Informationen sind wichtige Erkenntnisse, die in der Herstellung und Anwendung von Legierungen berücksichtigt werden können. Die Ergebnisse dieser Studie könnten wichtige Auswirkungen auf die Produktion und Anwendung der AA5083-H111 Legierung in Bereichen wie Luft- und Raumfahrt, Automobil- und Schiffbau haben.

SCHLÜSSELWÖRTER
AA5083-H111 Legierung, Gefüge, Korrosionsbeständigkeit, Korrosionsverhalten, Kurzzeit-Anlassprozess, Kühlumgebung

1 | INTRODUCTION

The AA5083 aluminum alloy finds widespread application across various industries, including automotive, aerospace, shipbuilding, rail transportation, and construction. This popularity is attributed to its notable features such as high weldability, corrosion resistance, good fatigue strength, and the ability to be cold-formed in the temper form [1–4]. In recent years, there has been a notable increase in its utilization within the defense industry for manufacturing armor, military foldable bridges, and personnel transport vehicles, owing to its lightweight nature and commendable performance under cyclic loads [1]. Additionally, the automotive sector has embraced this alloy for the production of welded tanks, structural components, and body construction. Similarly, in shipbuilding, it is employed for platforms, storage tanks, and pressure vessels, while also playing a crucial role in structural elements for railway transportation [2–3].

The AA5083 alloy can be hardened by heat treatment, although its effectiveness is lower compared to other aluminum alloys such as AA6061. The typical heat treatment process involves heating the alloy to a temperature between 500 °C to 540 °C and then quenching it in water. This process increases its strength but reduces its formability. To decrease the alloy's strength and increase its ductility, a heating (annealing) process can be applied. The specific process parameters and conditions may vary depending on the chemical composition of the alloy and the desired level of softening [5]. A common softening process for AA5083 involves annealing the alloy at 345 °C and then cooling it. Despite its superior properties, prolonged exposure to temperatures exceeding 150 °C, attributed to the presence of magnesium in its composition, induces changes in some of its properties such as corrosion resistance, hardness, and microstructure. This leads to the alloy softening or acquiring behavioral sensitivity, thereby losing its initial properties [2,4]. The magnesium phase in the structure tends to accumulate at grain boundaries and form β phases. This β phase, acting as an anode in the alloy, promotes intergranular corrosion and stress corrosion cracking. Hence, it is crucial to prevent or mitigate the loss of mechanical properties and corrosion damage caused by sensitivity [4]. The mechanical properties and corrosion resistance of the AA5083 alloy vary depending on the annealing process and process parameters [7].

At elevated annealing temperatures, the alloy's sensitivity state transitions to a stabilized state, causing the β precipitates to change from rod-like structures to spherical shapes within the structure [8]. The widths of Lüders bands in the cast AA5083 alloy, cooled in a salt bath after annealing, were influenced by both annealing temperature and heating rate [9]. Although increasing the annealing temperature reduces strength, the alloy remains suitable for traditional applications [10]. Plastic deformation of the AA5083 alloy follows the yield functions proposed by Barlat and Logan-Hosford, but does

not adhere to the criteria defined by Hill's or von Mises [11].

The understanding of the corrosion behavior of aluminum-magnesium alloys remains incomplete [12]. The homogenization process enhances the corrosion resistance of AA5083-H321 alloy, with a discernible improvement observed in both homogenized and non-homogenized alloys [13]. Recrystallization in AA5083 sheets, rolled at room temperature, initiates at temperatures of 260 °C and higher [14].

AA5083-H111 alloy is an aluminum alloy composed of elements such as aluminum, magnesium, and manganese. The corrosive behavior of this alloy is influenced by factors such as temperature, humidity, and chemical environment. Consequently, process parameters like tempering time and cooling medium can impact its corrosive response. While tempering time can enhance the alloy's strength, it also influences its susceptibility to corrosion. Research indicates that the corrosive behavior of AA5083-H111 alloy is sensitive to tempering time, with longer durations potentially leading to increased corrosion damage [15,16]. Moreover, the choice of cooling medium also affects the alloy's corrosive behavior. Higher cooling rates enhance the alloy's strength but alter its susceptibility to corrosion. Water cooling tends to exacerbate the corrosive behavior, whereas air cooling mitigates this effect.

In conclusion, the corrosive behavior of the AA5083-H111 alloy is influenced by various factors. Process parameters like tempering time and cooling medium play crucial roles in shaping its corrosive response and should be tailored to suit specific usage conditions. Thermal treatment exposes structural alloys to changes in mechanical and physical properties, as the energy involved can reshape their atomic structures at elevated temperatures. This phenomenon offers opportunities to tailor material properties according to desired specifications. Heating and cooling processes are commonly employed to enhance the mechanical properties and corrosion resistance of structural alloys [17]. Aluminum alloys, in particular, exhibit significant property modifications with variations in temperature and time. Tempering is a widely used technique for improving the mechanical properties and corrosion resistance of aluminum alloys [18]. This process helps prevent crack formation by reducing material stress and enhances durability. Moreover, tempering induces changes in the material's crystal structure, thereby increasing hardness and corrosion resistance [19–21]. Hence, studies investigating the impact of tempering on the hardness, corrosion resistance, and microstructure of the AA5083 alloy are essential for advancing our understanding of its behavior.

Tempering of aluminum alloys typically occurs at high temperatures and for extended durations, ranging from 12 hours to 240 hours. Despite this common practice, there remains a lack of comprehensive investigations into the corrosion behavior and microstructure of the alloy under varying annealing temperatures, durations, and cooling conditions [6,9,22]. Notably, studies specifically examining short-term tempering at annealing temperatures are notably absent from the existing literature. Therefore, the objective of this study is to explore the effects of tempering at 320 °C on properties such as hardness, corrosion resistance, and microstructure of AA5083 alloy. It is anticipated that the findings of this research will contribute significantly to filling this research gap.

2 | MATERIALS AND METHOD

2.1 | Materials and tempering process

In this study, commercial AA5083-H111 aluminum alloy sheet (Seykoç, Istanbul) was utilized. The conformity of the materials to the standard was verified using a Perkin Elmer Analyst 800 Atomic Absorption Spectrometer. Test specimens measuring of 6 mm×6 mm×50 mm were prepared from the AA5083 alloy sheet using a Brillant 240 cutting machine and an Optimum desktop milling machine (Germany). The specimens underwent gradual heating from room temperature to the tempering temperature of 320 °C at a heating rate of 10 °C/min in a Thermomac thermal processing oven, Figure 1a. Once the temperature reached 320 °C, the specimens were held for 30 minutes, 45 minutes, and 60 minutes, respectively. Subsequently, they were cooled using two different media: water and air, Table 1. The cooling water temperature was maintained at 20 °C, while the ambient air temperature stood at 23 °C.

TABLE 1 The parameters used in the study and sample codes.

Sample code	Tempering temperature (°C)	Tempering time (min.)	Cooling environment
S30	320	30	Water
S45	320	45	Water
S60	320	60	Water
H30	320	30	Air
H45	320	45	Air
H60	320	60	Air

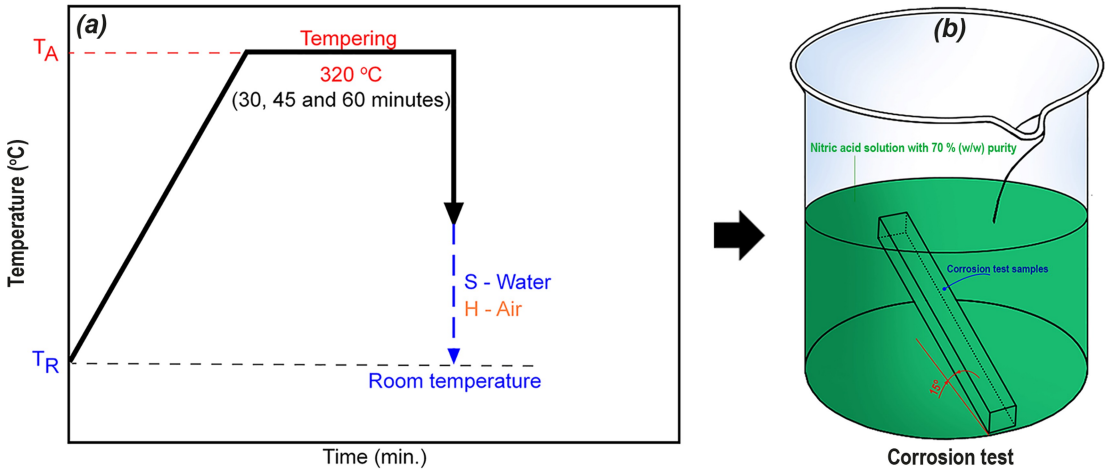

FIGURE 1 Schematic representation (a) tempering process and (b) corrosion test.

2.2 | Determination of material hardness

According to ISO 6506 standard, the hardness of the samples was determined using a Q250C model (ATM QNESS GMBH) universal hardness testing machine, employing the HBW 2.5/62.5 hardness scale. This scale utilizes a 2.5 mm ball diameter (D) and a nominal force (F) of 612.9 N, with a tungsten carbide ball-tipped indenter. The force is initially applied for 2 seconds, followed by a 15 second test force application. Subsequently, the diameter of the ball indentation (d) on the sample surface is measured. The Brinell hardness units (HB) are then calculated using Equation 1. For each parameter, three measurements were taken, and their averages were calculated.

$$\text{Brinell hardness} = \frac{0,102 \times 2F}{\pi D \times (D - \sqrt{D^2 + d^2})} \quad (1)$$

2.3 | Optical microscopy imaging

For microstructure examinations, the surfaces of the samples perpendicular to the rolling direction underwent successive sanding with 320 grit, 1100 grit, and 2400 grit silicon carbide papers. Subsequently, the surfaces were polished using 3 μm and 1 μm diamond paste applied with a felt cloth. Following polishing, the samples were etched with Keller's reagent. The microstructures were then observed under an Yamer MM-6000B model optical microscope at a magnification of 400x.

2.4 | Charpy impact test

To assess the ductile and brittle behavior of the samples quenched in water after the heat treatment, Charpy impact tests were performed in accordance with ISO 148-1 standard. An Instron MPX series 300 joule pendulum impact testing machine was utilized for the tests. During the test, 2 mm notches were introduced on the samples, and a 150° hammer angle was employed. The hammer energy applied was 5 J, and the tests were conducted at room temperature (23 °C).

2.5 | Tensile test

Tensile tests were carried out at Imkosan (Istanbul) using an Instron 5989 L2711 series premium grade 600 kN universal testing machine, in accordance with ASTM E8/E8 M-09 standard, at room temperature. During the experiments, the tensile speed was maintained at 5 mm/min. Calculations of tensile values, considered the dimensions of the specimens, including length and thickness.

2.6 | Three-point bending test

Bending tests were conducted following the guidelines outlined in ISO 7438 standard. A bending attachment connected to the Instron 5989 L2711 model 600 kN universal testing machine was utilized for the tests. During the tests, the specimens were positioned between two supports with a span of 64 mm. Bending was applied at a rate of 30 mm/min.

TABLE 2 Chemical composition of AA5083-H111 alloy.

Element, (%)	Si	Fe	Cu	Mn	Mg	Cr	Zn	Ti	Al
Standard	0.40	0.40	0.10	0.40–1.0	4.0–4.9	0.05–0.25	0.25	0.15	Balance
Based	0.15	0.33	0.07	0.48	4.20	0.07	0.13	0.05	Balance

2.7 | Determination of corrosion rate

The corrosion rates of the materials post-heat treatment were assessed following the ASTM G67-18 standard. Prior to testing, samples were weighed, and the area designated for corrosion exposure was calculated. The quantity of nitric acid specified in the standard (30 l/m^2) served as a reference for determining the appropriate amount of nitric acid based on the surface area of the samples. The samples underwent corrosion exposure in a closed beaker containing a 15° inclination, 30 °C temperature, and a 70% (weight/weight) purity nitric acid solution for a duration 24 hours, Figure 1b. Subsequently, the samples were removed from the beaker and subjected immersion in a 1 minute 80 °C sodium hydroxide solution followed by a 30 second 5% nitric acid solution for cleaning and removal of corrosion products from the surface. The samples were then rinsed with water and allowed to air dry. Following drying, the weight of the samples was measured, and the obtained results were compared with the initially measured values to determine the weight loss. The weight loss values obtained from the sample weighing were converted to the average corrosion rate using the Equation 2. In Equation 2, the constant K was taken as 8.76x104 (mm/yr). Here, KH represents the corrosion rate, T represents the exposure time in hours, A represents the area exposed to corrosion in cm^2, W represents the weight loss in grams, and D represents the density (g/cm^3).

$$KH = \frac{K\ x\ W}{A\ x\ T\ x\ D} \tag{2}$$

2.8 | Scanning electron microscope and energy-dispersive x-ray spectroscopy

The microstructures of the samples subjected to corrosion tests were examined using a Zeiss GeminiSEM 500 field emission scanning electron microscope operating at a voltage of 10 kV. Additionally, the chemical composition of the samples was analyzed using the energy-dispersive x-ray spectroscopy technique on the same device.

3 | RESULTS AND DISCUSSIONS

3.1 | Chemical composition

The alloy's chemical content, conforms to the standard and falls within the specified limit values, Table 2. Ensuring compliance with the standard's chemical composition requirements is essential for accurately interpreting test results. The AA5083 alloy, with a magnesium ratio 4.2%, meets the chemical composition criteria of the 5000 series aluminum-magnesium alloys group. This group typically contains 4% to 5% magnesium by weight and is renowned for its high corrosion resistance. This adherence to standards enhances the reliability of the alloy's performance across various applications.

3.2 | Hardness measurements

The initial hardness of the untempered samples measured at 71.2 Brinell hardness serves as a baseline for the subsequent analysis. Interestingly, both the choice of cooling medium and the duration of tempering are found to significantly influence hardness, Table 3. With increasing tempering time, a clear trend emerges: a reduction in hardness, resulting in larger indentation diameters, Figure 2a. Samples subjected to a 30-minute tempering process (S30 and H30) exhibit the highest hardness values among all samples. However, a nuanced pattern emerges as tempering time extends; at 45 minutes, a decrease in hardness is observed, followed by a subsequent increase at the 60-minute mark. Notably, the air-quenched samples show a more substantial increase in hardness compared to other cooling media,

TABLE 3 Numerical data of hardness measurement.

Sample code	Brinell hardness	d_1 (mm)	d_2 (mm)	Standard deviation
S30	111 (±2)	0.829	0.839	1.00
S45	92.40 (±1.2)	0.913	0.910	0.62
S60	92.83 (±1.4)	0.906	0.913	0.70
H30	96.43 (±0.7)	0.892	0.894	0.38
H45	86.63 (±1.5)	0.941	0.939	0.76
H60	90.30 (±1.8)	0.922	0.922	0.92

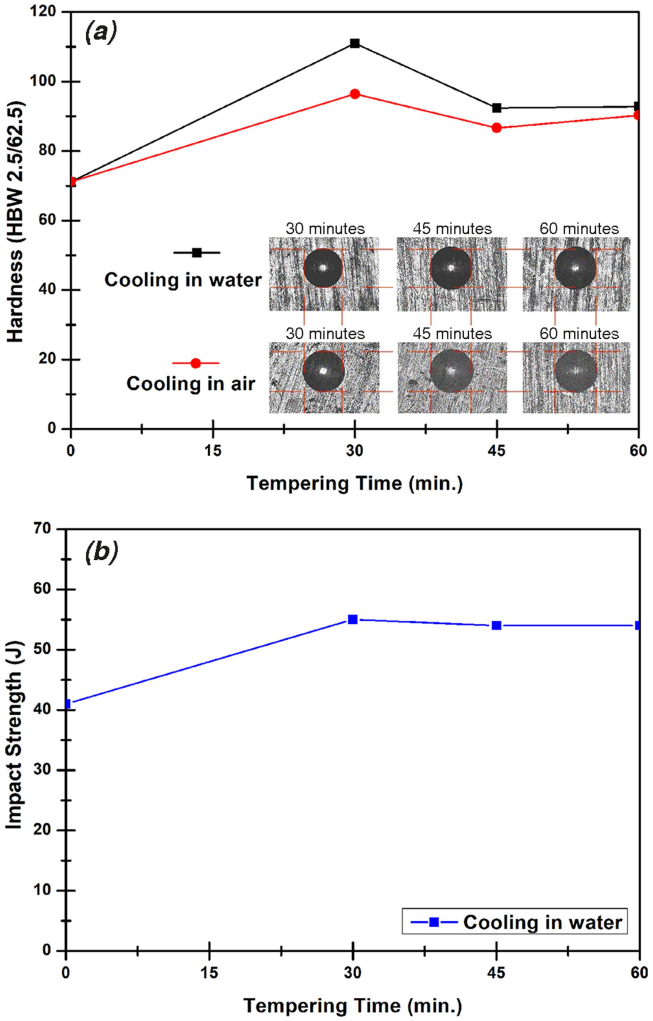

FIGURE 2 Hardness and impact strength changes (a) Hardness and (b) Charpy impact strength.

emphasizing the importance of the quenching process. These findings are supported by the demonstration of successful tempering, evident from the low standard deviation and minimal differences in hardness range, Table 3. This underscores the intricate interplay between tempering parameters and resultant hardness, underscoring the importance of carefully optimizing the tempering process to achieve desired material properties.

3.3 | Charpy notch impact test results

The impact strength, initially measured at 41 Joules in the sample without tempering, exhibited a remarkable 34% increase with tempering. The highest impact strength value, reaching 55 Joules, was achieved with a 30-minute tempering time, Figure 2b. Surprisingly, despite variations in tempering time, there was no significant upward trend in impact strength values.

One noteworthy observation is the transition in fracture forms: from a ductile manner observed in the sample without tempering to a brittle fracture form in the tempered samples. This intriguing shift suggests that the water quenching process following tempering, and the resultant microstructure, exert a notable influence on these fracture forms. The pronounced impact strength improvement and the alteration in fracture behavior underscore the intricate relationship between tempering parameters, microstructural changes, and material properties, reinforcing the importance of a comprehensive understanding for optimizing tempering processes.

3.4 | Tensile test results

The tensile strength, initially measured at 275 MPa in the untreated sample, underwent a noteworthy increase with tempering, reaching a maximum of 305 MPa, as detailed, Table 4. Specifically, the sample labeled as S60 demonstrated the highest tensile strength after the tempering process, showcasing an impressive 11% enhancement. Interestingly, the tempering process exerted a positive impact on the tensile strength across all samples, highlighting its role in enhancing material properties. However, an intriguing observation emerged during the tensile process for tempered samples; a brittle fracture occurred, Figure 3a. This shift in fracture behavior, from ductile to brittle, underscores the complex interplay between tempering conditions and material response. Moreover, fracture elongation values in tempered samples were significantly lower compared to the untreated sample, emphasizing the trade-off between strength and ductility associated with tempering. While the difference between the yield strength values of heat-treated specimens and untreated specimens was not excessively high, a nuanced increase was observed as tempering time extended. This finding, although not significantly pronounced, adds an additional layer to the understanding

TABLE 4 Numerical data of tensile test results.

Sample code	Yield strength (MPa)	Tensile strength (MPa)	Elongation (%)
Reference	125	275	22.00
S30	128	285	1.43
S45	133	293	1.22
S60	142	305	0.98
H30	126	278	1.74
H45	128	284	1.51
H60	130	287	1.34

FIGURE 3 Application of tensile and three-point bending tests and the appearance of specimens after testing (a) Tensile test and (b) Three-point bending test.

of the tempering process and its impact on material properties. The overall consistency of the obtained results with existing literature further strengthens the validity of the findings [23, 24], providing valuable insights for future investigations into optimizing tempering conditions for improved material performance.

3.5 | Three-point bending test results

In the bending test, a critical observation unfolded as all materials underwent fracture, as visually, Figure 3b. Notably, upon closer examination, it became apparent that cracks had formed on the fracture surfaces, indicative of the intricate nature of the bending process. The fractures occurred rapidly, further emphasizing the dynamic response of the materials under bending stress. Interestingly, yielding was observed to take place after the application of 15 MPa in the specimens. However, a notable challenge arose during the testing procedure, as the fracture occurred before yielding could be fully realized. This unique circumstance posed a limitation, preventing the determination of specific bending strength values. This highlights the importance of meticulous testing methodologies and the necessity for comprehensive analysis, especially in scenarios where the fracture behavior is rapid and intricate, as observed in this bending test.

3.6 | Corrosion rate

The analyses conducted play a pivotal role in the comparative assessment of corrosion resistance among various alloys. Overall, all samples exhibit commendable corrosion resistance, characterized by low corrosion rates. Notably, sample S60 stands out as the top performer, boasting the lowest corrosion rate (0.047 mm/yr) and minimal mass loss (5.20%). Conversely, sample H30 demonstrates the least favorable performance, with the highest corrosion rate (0.088 mm/yr) and mass loss (9.74%). The elevated magnesium content in sample H30 is identified as a potential contributor to its diminished corrosion resistance [25–28]. Interestingly, samples S45 and H45, as well as S30 and H60, showcase comparable performance, Table 5. Lower corrosion rates and minimal mass loss in these samples underscore improved corrosion resistance, emphasizing the multifaceted influence of alloy composition, tempering conditions, and time on corrosion behavior.

Despite the conventionally used approach of utilizing material hardness to assess corrosion rates, a nuanced observation arises in the presented examples. For instance, sample S60 exhibits higher hardness yet a lower corrosion rate compared to other samples, while sample H45, with lower hardness, also boasts a lower corrosion rate, Figure 4. This discrepancy suggests that factors such as chemical composition, surface roughness, and electrochemical potential play pivotal roles in determining corrosion rates [29–37]. The data indicates that hardness alone is insufficient for the comprehensive evaluation of corrosion rate, and a thorough analysis of material properties is imperative. These findings align with earlier studies, reinforcing the notion that hardness has minimal impact on corrosion behavior, while material composition exerts a more pronounced influence [38–40]. In conclusion, while hardness remains a valuable parameter, it must be considered in conjunction with other factors for a holistic assessment of corrosion behavior and material properties.

TABLE 5 Numerical data of corrosion rate measurement.

Sample code	Corrosion rate (mm/yr)	Mass loss (g)	Mass loss (%)
S30	0.078	0.416	8.63
S45	0.059	0.315	6.53
S60	0.047	0.251	5.20
H30	0.088	0.470	9.74
H45	0.067	0.358	7.42
H60	0.053	0.283	5.87

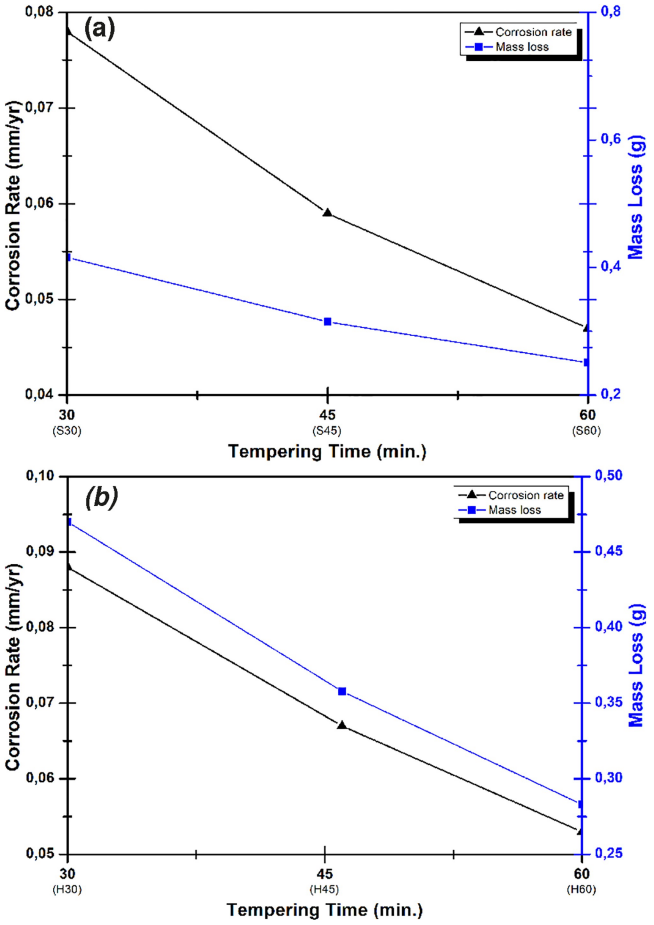

FIGURE 4 The variation of corrosion rate and mass loss with tempering time and air-cooling environment.

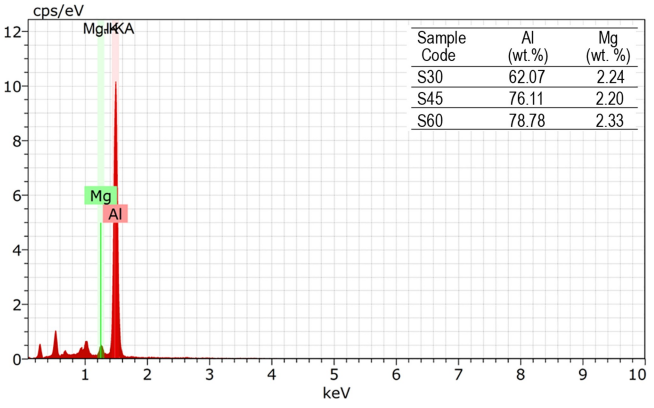

FIGURE 5 Energy-dispersive x-ray spectroscopy chart.

3.7 | Energy-dispersive x-ray spectroscopy analysis

The insights derived from the energy-dispersive x-ray spectroscopy analysis play a pivotal role in comprehending the mass losses incurred by the material due to corrosion, Figure 5. The nuanced details brought to light by the analysis unveil intriguing variations in the

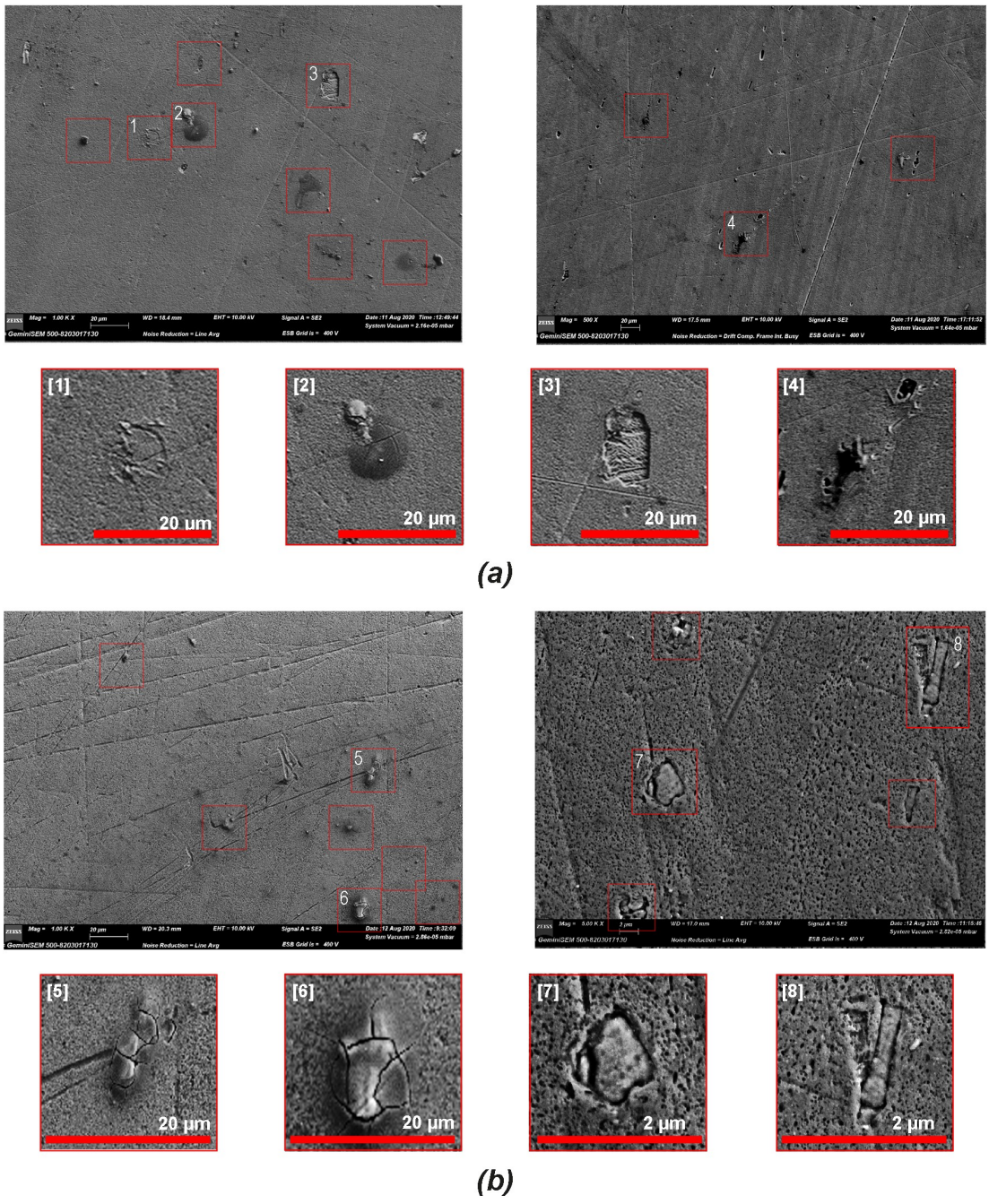

FIGURE 6 Scanning electron microscope image (a) S30 and (b) H30.

aluminum and magnesium contents among the S30, S45, and S60 samples, hinting at the potential effects of tempering and water quenching on the alloy composition. Specifically, the S30 sample stands out with lower aluminum and magnesium contents, suggesting fewer composition changes after 30 minutes of tempering. On the other hand, the S45 and S60 samples exhibit comparable aluminum and magnesium contents, with the S60 sample showcasing a higher aluminum content. This observation aligns with corrosion rate studies that have previously established a correlation between magnesium content and corrosion rate in aluminum-magnesium alloys [41–45]. The correlation between the energy-dispersive x-ray spectroscopy analysis results and the corrosion rate data becomes evident, underscoring the influence of tempering time on aluminum mass loss rates. This correlation further accentuates the intricate relationship between alloy composition adjustments during tempering and subsequent corrosion behavior. The incorporation of energy-dispersive x-ray spectroscopy analysis enriches our understanding of the underlying mechanisms contributing to corrosion, shedding light on the

alloy's compositional changes and their impact on material degradation over time.

3.8 | Scanning electron microscope microstructure imaging

The manifestation of corrosion at the grain boundaries provides a visual cue, underscoring the interplay between surface and structural properties on corrosion behavior. Both samples showcase distinctive pit formations, encompassing a spectrum from small holes to larger pits. These formations arise from localized depressions and subsequent electrochemical reactions, as elucidated in prior studies [46–49]. The initiation of corrosion at as small points, progressing deeper and causing material loss, is a noteworthy observation. Particularly striking is the comparative between the air-cooled H30 sample and the water-cooled S30 sample, Figure 6a, b. Evidently, the air-cooled H30 sample exhibits a more rapid onset and progression of corrosion compared to it water-cooled counterpart. This visual distinction in surface morphology correlates seamlessly with the mass loss and corrosion rate data garnered from the tests, reinforcing the interrelation between observed surface features and quantitative corrosion metrics. The rates obtained from the corrosion tests not only validate the surface morphology findings but also contribute to a comprehensive understanding of the corrosion progression. This coherence between visual assessments and quantitative data enhances the reliability of the corrosion study results, emphasizing the significance of considering both surface morphology and corrosion rates in evaluating material performance under corrosive conditions.

4 | CONCLUSIONS

This comprehensive study encompasses experimental findings across five key domains: hardness measurements, tensile strength, three-point bending strength, Charpy impact test results, and corrosion rate analysis. The hardness measurements revealed a consistent reduction in material hardness with increasing tempering time, accompanied by a corresponding expansion in ball diameter. Air-cooled samples exhibited the lowest hardness values, while the most elevated values were achieved in samples denoted as S30 and H30, both tempered for a duration of 30 minutes. Charpy impact test results demonstrated a notable 34% improvement in the material's impact resistance post-tempering, with the optimum impact resistance observed in samples subjected to a 30-minute tempering period. The alterations in fracture behavior during tensile tests, along with the derived tensile strength values, underscore the profound impact of tempering time and cooling medium on the material's durability and tensile properties. In the three-point bending test, yielding was identified after reaching 15 MPa, yet rapid crack formation prevented the calculation of bending strength values. This complex behavior in fracture patterns for the AA5083 alloy following tempering and cooling processes emphasizes the necessity for a thorough and intricate analysis. Corrosion rate measurements revealed commendable corrosion resistance across all samples, with the S60 sample exhibiting superior performance characterized by the lowest corrosion rate and weight loss. Conversely, the H30 sample displayed the highest corrosion rate and weight loss. Collectively, these findings affirm the efficacy of the tempering process in enhancing both the mechanical properties and corrosion resistance of the AA5083 alloy.

DATA AVAILABILITY STATEMENT

The raw data required to reproduce these findings can be obtained from the authors via email.

ORCID

İ. Karagöz http://orcid.org/0000-0002-2644-8511

REFERENCES

1. S. Gürgen, *Politeknik Dergisi* **2019**, *22*, 293.
2. R. J. Mills, B. Y. Lattimer, S. W. Case, A. P. Mouritz, *Corros. Sci.* **2018**, *143*, 1.
3. M. Ma, J. Zhang, D. Yi, B. Wang, *Int. J. Fatigue* **2019**, *126*, 357.
4. S. Liu, X. Wang, Y. Tao, X. Han, C. Cui, *Appl. Surf. Sci.* **2019**, *484*, 403.
5. ASM Handbook Committee, Heat treating of aluminum alloys. ASM Handbook 4, A. B. D., **1999**.
6. Z. Tang, F. Jiang, M. Long, J. Jiang, H. Liu, M. Tong, *Appl. Surf. Sci.* **2020**, *514*, 146081.
7. S. Lin, Z. Nie, H. Huang, B. Li, *Mater. Des.* **2010**, *31*, 1607.
8. Y. Ding, K. Gao, H. Huang, S. Wen, X. Wu, Z. Nie, S. Guo, R. Shao, C. Huang, D. Zhou, *Mater. Des.* **2019**. *174*, 10778.
9. S. L. Xia, M. Ma, J. X. Zhang, W. X. Wang, W. C. Liu, *Mater. Sci. Eng. A* **2014**, *609*, 168.
10. H. Fang, H. Liu, Y. Yan, X. Luo, X. Xu, X. Chu, Y. Lu, K. Yu, D. Wang, *Mater. Sci. Eng. A* **2021**, *804*, 140682.
11. T. Naka, Y. Nakayama, T. Uemori, R. Hino, F. Yoshida, *J. Mater. Process. Technol.* **2003**, *140*, 494.
12. A. Alil, M. Popović, T. Radetić, M. Zrilić, E. Romhanji, *J. Alloys Compd.* **2015**, *625*, 76.
13. Y. Huang, Y. Li, Z. Xiao, Y. Liu, Y. Huang, X. Ren, *J. Alloys Compd.* **2016**, *673*, 73.
14. Z. Li, D. Yi, C. Tan, B. Wang, *J. Alloys Compd.* **2020**, *817*, 152690.
15. L. Lokas, V. Alar, *Mater. Corros.* **2019**, *70*, 1817.
16. D. Uz, M. M. Solomon, H. Gerengi, M. Sahin, M. Yıldız, *Mater. Res. Express* **2021**, *8*, 076516.

17. J. Haigen, X. Kemou, Y. Xiamoei, M. Chengji, *Microstructures* **2021**, *10*, 410.
18. J. Li, Y. He, X. Zhao, C. Kim, *Coating* **2022**, *12*, 787.
19. S. Chen, K. Chen, P. Dong, S. Ye, L. Huang, *Trans. Nonferrous Met. Soc. China* **2014**, *24*, 2320.
20. D. Feng, X. M. Zhang, S. D. Liu, T. Wang, Z. Z. Wu, Y. W. Guo, *Mater. Sci. Eng. A* **2013**, *588*, 34.
21. A. Dhal, S. K. Panigrahi, M. S. Shunmugam, *J. Alloys Compd.* **2017**, *726*, 1205.
22. F. H. Cao, V. H. Len, Z. Zhang, J. Q. Zhang, *Russ. J. Electrochem.* **2007**, *43*, 837.
23. J. Li, Q. Zeng, X. Y. Wen, T. Zhai, *Mater. Sci. Technol.* **2007**, *23*, 225.
24. L.-E. Svensson, L. Karlsson, H. Larsson, B. Karlsson, M. Fazzini, J. Karlsson, *Sci. Technol. Weld. Joining* **2000**, *5*, 285.
25. L. Xu, X. Liu, K. Sun, R. Fu, G. Wang, *Materials* **2022**, *15*, 2613.
26. D. Luo, F. Li, G. Xing, *Rev. Adv. Mater. Sci.* **2022**, *61*, 638.
27. H. Ezuber, A. El-Houd, F. El-Shawesh, *Mater. Des.* **2008**, *29*, 801.
28. C. Li, Y. Zhao, J. Liu, J. Xu, D. Guo, H. Zhang, X. Zhou, P. Yang, S. Zhang, *Crystals* **2023**, *13*, 506.
29. A. Musza, D. Ugi, A. Vida, N. Q. Chinh, *Coating* **2022**, *12*, 1528.
30. W. Handoko, F. Pahlevani, V. Sahajwalla, *Materials* **2018**, *11*, 2404.
31. I. Sudhakar, Y. V. Vardhan, P. Sruthi, P. V. S. Harshit, S. S. Kumar, V. V. Prakash, *Mater. Today: Proc.* **2018**, *5*, 3919.
32. O. I. Olabisi, A. A. G. Olorunnishola, *Int. J Emerging Trends in Eng. Dev.* **2019**, *9*, 7.
33. İ. Karagöz, *El-Cezeri* **2019**, *6*, 748.
34. Y. Kim, M. Yo, M. S. Moon, *Materials* **2020**, *13*, 4211.
35. G. Chi, D. Yi, H. Liu, *J. Mater. Res.* **2020**, *9*, 1162.
36. N. N. Khobragade, A. V. Bansod, K. V. Giradkar, A. P. Patil, K. Jagtap, R. Pawde, A. P. Moon, *Mater. Res. Express* **2018**, *5*, 015403.
37. R. Galo, R. F. Ribeiro, R. C. S. Rodrigues, L. A. Roch, M. G. C. Mattos, *Braz. Dent. J.* **2012**, *23*, 141.
38. C. Escrivà-Cerdán, S. W. Ooi, G. R. Joshi, R. Morana, H. K. D. H. Bhadeshia, R. Akid, *Corros. Sci.* **2019**, *154*, 36.
39. D. A. López, T. Pérez, S. N. Simison, *Mater. Des.* **2003**, *24*, 561.
40. A. Klyszewski, J. Zelechowski, M. Opyrchal, M. Nowak, A. Frontczak, P. Rutecki, ICAA13 Pittsburgh. Springer, Cham. **2012**.
41. J. Y. Chang, A. Shan, *Materials* **2003**, *347*, 165.
42. S. O. Adeosun, O. I. Sekunowo, S. A. Balogun, V. D. Obiekea, *Int. J. Corr.* **2012**, 927380.
43. X. Zhang, K. Zhang, X. Deng, L. Hongwei, L. Yongjun, M. Minglong, L. Ning, Y. Wang, *Prog. Nat. Sci.* **2012**, *22*, 169.
44. Y. Shaohua, Z. Dancheng, T. Yabin, Y. Changmei, Z. Yujuan, L. Linshan, *Nonferrous Met. Sci. Eng.* **2018**, *9*, 1.
45. Y. Wang, H. Liao, Y. Wu, J. Yang, *Mater. Des.* **2014**, *53*, 634.
46. P. Zhu, X. Cao, W. Wang et al, *J. Mater. Res.* **2017**, *32*, 3904.
47. G. C. Y. Yang, W. T. Tsai, *Corr. Sci. Technol.* **2002**, *31*, 361.
48. Z. S. Smialowska, *Corros. Sci.* **1999**, *41*, 1743.
49. M. C. Reboul, T. J. Warner, H. Mayet, B. Baroux, *Corr. Rev.* **1997**, *15*, 471.

How to cite this article: İ. Karagöz, M. Buğdaycı, L. Öncel, *Materialwiss. Werkstofftech.* **2024**, *55*, e202300217. https://doi.org/10.1002/mawe.202300217